A Functional Region-based Approach for the Numerical Simulation of Patient-specific Cerebral Blood Flows with Clinical Validation

Zhengzheng Yan, Rongliang Chen, Fenfen Qi, Xiao-Chuan Cai

Abstract—Objective: Imposing accurate outflow boundary conditions remains a significant challenge in 3D computational fluid dynamics simulations of patient-specific cerebral blood flow. Widely used Windkessel models often rely solely on geometric factors, such as outlet numbers and diameters, leading to inaccuracies caused by image quality limitations and simplified vessel representations. This preliminary study proposes a novel functional region-based approach to enhance the accuracy of cerebral blood flow simulations. Methods: Cerebral vessels were divided into functional regions by combining population-based cerebral blood flow distributions with patient-specific arterial geometries from medical images. Within each functional region, parameters of Windkessel models for individual outlets are calculated based on their corresponding diameters/areas, accounting for both functional and geometric characteristics. Validation was conducted on a single subject using clinical Transcranial Doppler ultrasound data, with comparisons made to a conventional area-based approach. Results: The functional region-based approach demonstrated better alignment with clinical measurements, outperforming the area-based method in velocity profiles at 5 of 7 monitored locations. It also provided closer agreement with measured blood flow distribution, with maximum percentage differences of -4.5%. Conclusion: By integrating vascular geometry and functional perfusion data, the proposed approach provides a physiologically informed strategy for setting outlet boundary conditions in cerebral blood flow simulations. Significance: Although demonstrated in a single-subject case, this approach shows potential to improve patient-specific simulation reliability by reducing errors caused by imaging artifacts and geometric simplifications, offering value for future clinical and research applications.

Index Terms—Cerebral blood flow simulation, lumped parameter model, computational fluid dynamics, patient-specific

I. INTRODUCTION

Computational fluid dynamics (CFD) is increasingly employed as a tool to study patient-specific cerebral hemodynamics in order to understand certain cerebral diseases and plan treatments [1]–[3]. In 3D CFD simulations of cerebral blood flow (CBF), the arterial geometry is reconstructed from medical imaging data such as MRI or CT scans. Considering image resolution and computing limitations, the vessel model is truncated at distal branch ends rather than using the fully-resolved arterial geometry [4]. Accurate outflow boundary conditions are needed to simulate the downstream vascular bed influence on the modeled domain and reflect macroscopic CBF characteristics. In cerebral blood flow, autoregulation is an important and specific mechanism to maintain adequate perfusion and oxygen supply to the brain [5]. The Circle of Willis (CoW) structure, along with leptomeningeal anastomoses connecting the terminal cortical branches of major intracranial arteries, are considered the crucial anatomical features contributing to autoregulation [6]. Research suggests that the CoW can maintain blood flow perfusion to distal branches in the event of occlusion of major intracranial arteries, while leptomeningeal anastomoses can sustain perfusion in the event of occlusion of distal small branches [7]. In 3D CBF simulation, the CoW structure is generally incorporated and appropriate outflow boundary conditions are needed to simulate the downstream vascular influence, including the autoregulatory function of leptomeningeal anastomoses, particularly in cases of vessel occlusion.

The zero-dimensional or lump-parameter Windkessel models, originally derived from electrical circuit theory and first applied in the cardiovascular system, are the most commonly used as the boundary conditions in 3D CBF simulations [8]. In the original two-element Windkessel model, the vessel network is considered as an electric circuit consisting of a resistor and a capacitor, which characterize the arterial peripheral resistance and the vessel compliance, respectively. Later, more sophisticated lumped parameters models including the three-element Windkessel model (WK3, with additional parameter for the characteristic impedance) and the four-element Windkessel model (with the arterial inertance) were developed [9]. Among the Windkessel models, the WK3 has been shown to be a good physiologically-based model of the arterial system [8]. Although there are some shortcomings such as errors in the low-frequency range, WK3 suffices for most studies in the clinical cerebral hemodynamic analysis [10]–[12]. We therefore will focus on improvement of WK3 in the rest of the paper.

In the WK3 model, the vascular bed downstream of the modeled domain is represented by an electric-circuit consisting of a proximal resistance (R_p), a distal resistance (R_d), and a capacitance (C). In simplified forms of vessel elasticity, flow resistance and intracranial pressure, these parameters reflect the macroscopic CBF autoregulation [13]. The autoregulation

Zhengzheng Yan and Rongliang Chen are with Shenzhen Institutes of Advanced Technology, Chinese Academy of Sciences, Shenzhen, China.

Fenfen Qi is with the Department of Mathematics, University of Macau, Macau, PR China

Xiao-Chuan Cai is with the Department of Computer Science, University of Colorado Boulder, Boulder, USA (e-mail: cai@colorado.edu).

is governed by coupled multiphysics interactions across the cellular, tissue, and organ scales [14], [15]. Correspondingly, the values of WK3 parameters depend on patient-specific physiological properties such as blood vessel diameter, length, Young's modulus, downstream flow viscosity, etc [16], [17]. In the case of multiple outlets, each branch outlet needs an individual value of RCR (R_p-C-R_d) to provide an acceptable hemodynamic characterization. The patient-specific values require parameter adjustment through in-vivo data, thereby improving consistency with physiological measurements. If possible, direct measurements of these parameters are preferred since the accuracy of imposed boundary conditions affect the numerical results significantly [18]. Unfortunately, patient-specific WK3 parameters are often unavailable from measurements in practice [19], necessitating mathematical descriptions, e.g., Murray's Law [20], [21], to identify the resistance and compliance for each outlet based on their areas or diameters.

However, the area-based approach for assigning Windkessel parameters has several key disadvantages. Foremost, it demonstrates poor ability to adequately reflect functional and regional differences in cerebral blood flow regulation, which are crucial for allowing subtle therapeutic modulation of blood flow in different conditions or brain areas at the capillary and arteriolar levels [22], [23]. Black et al. [24], [25] have demonstrated a approach to calibrate WK3 model parameters using 4D Flow-MRI data to derive patient-specific boundary conditions for CFD simulations, particularly in large arteries such as the aorta. However, the spatial resolution and velocity encoding range of current 4D Flow-MRI remain challenges for CBF simulation, especially in smaller and more tortuous intracranial vessels [26].

For instance, when specific brain regions undergo functional abnormalities like ischemic stroke or Alzheimer's disease, accounting for functional and regional parameters becomes especially critical. Secondly, the number and areas of reconstructed outlets heavily depend on image quality and the segmentation process, which can be challenging to control in practice, especially when the diameter of distal arteries approaches the hardware resolution limits of imaging modalities(around 0.1-1.0 mm, for CT or 3T MRI). Imaging artifacts such as uneven contrast dye distribution may prevent the reconstruction of many small vessels. Moreover, clinical studies have shown that including more distal blood vessels can improve the accuracy of CFD simulations [27]. However, pixel size often determines the diameter of the reconstuctable distal blood vessels, resulting in very similar diameters or areas for all vessel outlets. Clearly, parameters obtained by area-based approach also yields very similar results, making it impossible to accurately capturing the differentiated functional characteristics of the downstream vascular network for each truncated outlet.

To address these limitations, this study proposes a functional region-based approach to improve the assignment of the RCR parameters of Windkessel model using more physiological information of the vessel, namely the functional region of the brain corresponding to each blood vessel. Toward this goal, after rebuilding the patient-specific arterial model, we first classify all outlets into several groups according to their upstream vascular locations, and the blood flow to each group is determined by regions following a known population-specific CBF distribution. While inter-subject variability exists, population-averaged CBF maps provide a practical substitute for regional perfusion when individual data are unavailable. They enable consistent incorporation of functional constraints into boundary condition assignment. Then, in each region, the flow distribution and the parameters for individual outlets are determined by their corresponding areas as in the standard approach. Different from the current area-based assignment, this two-step method accounts for both functional regions and geometric characteristics. The effectiveness of the proposed approach is demonstrated by a case study, where numerical results are compared against clinical measurements from Transcranial Doppler (TCD) ultrasonography. The results show that the predicted velocity profiles match clinical data well, with improved accuracy over the traditional area-based method.

In clinical settings, certain diagnostic or treatment decisions, such as evaluating collateral redistribution after ICA stenosis, are robust to moderate uncertainty in absolute velocity estimates. Flow direction and asymmetry often matter more [28]. The proposed approach may thus support rapid cerebrovascular risk assessment or treatment planning, particularly when perfusion imaging is unavailable or time-limited.

The rest of the paper is organized as follows. Section II introduces a detailed numerical simulation method and steps for assigning the resistance and compliance to each outlet. Section III and Section IV presents the numerical experiments as well as the discussion. Some limitations and conclusions of our work are contained in Section V and Section VI, respectively.

II. Materials and methods

A. Patient-specific morphological domain and physiological data measurement

The subject of this study is a carefully screened healthy volunteer. Although the study is observational and the collected data are fully anonymized, written informed consent was obtained from the subject prior to participation. High-resolution multi-slice magnetic resonance angiography (MRA) images are used for the subject-specific morphological domain segmentation. The images are acquired on an MR scanner at 3T (Siemens Verio) for intracranial arteries. The main acquisition parameters are: pixel spacing of 0.39 mm, slice thickness of 0.80 mm, image resolution of 512×512, repetition time/echo time (TR/TE) = 23/3.5 ms, flip angle of $18°$, and 222 contiguous slices. All blood vessels with a diameter larger than 1.0 mm are reconstructed and checked by experienced clinicians to confirm that it is consistent with the patient's anatomy, as shown in Fig. 1. The reconstructed cerebral artery tree includes four large arteries: the right and left internal carotid arteries (ICA) and the right and left vertebral arteries (VA). The vessel geometry also incorporates the iconic Circle of Willis, which gives rise to three pairs of main arteries: the anterior cerebral arteries (ACA), the middle cerebral arteries (MCA), and the posterior cerebral arteries (PCA).
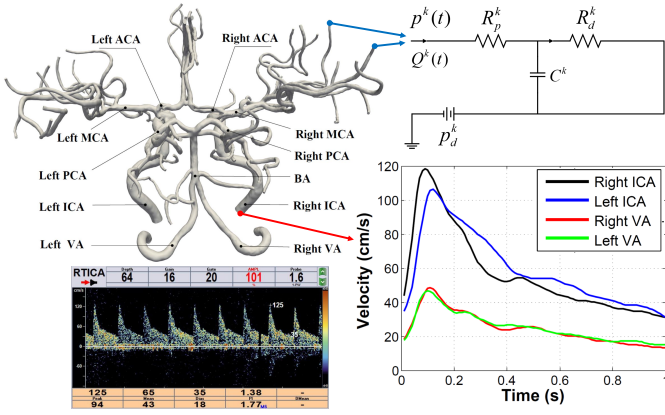
Fig. 1: Reconstructed subject-specific cerebral artery tree with inflow and outflow boundary conditions. A total of 11 measuring points are marked at different vessel segments, and the velocities and pressures at these locations are used for comparison. The velocity profiles at ICA and VA are extracted from the TCD ultrasound data for constructing inflow boundary conditions (shown in the lower right sub-figure), while a color-coded TCD image of the right ICA is shown as an example in the lower left sub-figure. A three-element lumped parameter Windkessel model is imposed on the outlet boundary (indicated in the top right sub-figure).

To validate the computational results, we use the flow rates measured with TCD ultrasound which can be used non-invasively to monitor the blood flow velocity in real-time. The TCD measurements were performed with a 1.61 MHz probe (EPIQ 5, Philips) through the temporal bone window, with insonation depths ranging from 55-100 mm depending on vessel location. The velocity values at 11 major vessel segments, shown in Fig. 1 are recorded, and the values at the left and right ICA, the right and left VA are used as the inflow boundary conditions, and the values at the other 7 segments (BA, left and right ACA, left and right MCA, and left and right PCA) are used to validate the computational results.

B. Governing equations and boundary conditions

We assume the blood flow in the cerebral artery is Newtonian with a constant dynamic viscosity $\mu = 0.0037 \ \mathrm{Pa \cdot s}$ and density $\rho = 1.050 \ \mathrm{g/cm^3}$. The Reynolds number for the middle cerebral artery was estimated to be approximately 342, using a characteristic diameter of 3.5 mm and an average velocity of 40 cm/s. Consequently, all simulations were conducted under the assumption of laminar flow. From the conservation laws of mass and momentum, the governing equations of the unsteady blood flow in the cerebral artery are expressed as:

$$\rho \left(\frac{\partial \mathbf{u}}{\partial t} + \mathbf{u} \cdot \nabla \mathbf{u} \right) = \nabla \cdot \sigma + \mathbf{f} \quad \text{in} \quad \Omega,$$
$$\nabla \cdot \mathbf{u} = 0 \quad \text{in} \quad \Omega, \tag{1}$$

where $\mathbf{u}$ is the velocity vector, p is the pressure, $\sigma = -p\mathbf{I} + \mu(\nabla \mathbf{u} + (\nabla \mathbf{u})^T)$ is the Cauchy stress tensor, and $\mathbf{I}$ is a 3×3 identity matrix. $\mathbf{f}$ is the external force. Ω is the arterial domain bounded by the wall Γ_W, inlets Γ_I and outlets Γ_O.

A non-slip boundary condition is imposed on Γ_W with the rigid wall assumption,

$$\mathbf{u} = 0, \quad \text{on} \quad \Gamma_W. \tag{2}$$

Γ_I consists of four inlets, and a transient pulsatile blood velocity $\mathbf{g}^i$ is prescribed on each of the inflow boundary Γ_I^i, representing the left and right ICA, the left and right VA, where $i = 1, 2, 3, 4$,

$$\mathbf{u}^i = \mathbf{g}^i \quad \text{on} \quad \Gamma_I^i. $$

For each inlet, the temporal waveform of $\mathbf{g}^i$ is obtained from the TCD ultrasound data and some representative pulsatile blood flow waveforms are shown in Fig. 1. Note that the TCD presents a spectral waveform with peak systolic velocity (PSV) and end diastolic velocity (EDV) values, and (PSV + 2EDV)/3 is a surrogate mean flow velocity (MFV) on the cross-section where the measurement point is placed [29]. Based on this assumption, we then obtain $\mathbf{g}^i$ by MFV and the TCD waveform for each inlet Γ_I^i (see Fig. 1).

Three-element Windkessel model-based condition is imposed on each outlet [30], [31]. As shown in Fig. 1, a proximal resistance R_p, a distal resistance R_d and a compliance C are introduced to describe the hemodynamics of the distal cerebral system function. Specifically, based on Kirchhoff's laws and Ohm's law, the WK3 model relates the blood pressure and the flow rate by the following ordinary differential equation on the k-th outlet,

$$C^k \frac{dp^k(t)}{dt} + \frac{p^k(t)}{R_d^k} = R_p^k C^k \frac{dQ^k(t)}{dt}$$
$$+ Q^k(t) + \frac{R_p^k}{R_d^k} Q^k(t) + \frac{p_d}{R_d^k}, \tag{3}$$

where C^k and R_p^k represent the systemic compliance and resistance of the arteries leading to the k-th outlet, $p^k(t)$ and $Q^k(t)$ are the time-varying blood pressure and flow rate at time t. R_d is the resistance associated with the peripheral cerebrovascular bed. p_d is the intracranial pressure assumed to be 15 mmHg. Solving Eq. (3), we obtain the pressure value $p^k(t)$ at the k-th outlet,

$$p^k(t) = [p^k(0) - R_p^k Q^k(0) - p_d]e^{-\frac{t}{\tau^k}} + p_d$$
$$+ R_p^k Q^k + \int_0^t \left(\frac{e^{-(t-s)/\tau}}{C^k} \right) Q^k(s)ds, \tag{4}$$

where $\tau^k = R_d^k C^k$.

C. Classification of outlets in terms of functional regions

In Eq. (4), the parameters R_p^k, C^k, and p_d approximately represent the function of the small arteries and arterioles that are removed by the lack of resolution of the imaging process. Appropriate outflow boundary conditions and the corresponding physiological conditions rely on the accuracy of these parameters. Unfortunately, the parameters are usually difficult to obtain by direct measurements in practice. One of the commonly used methods [32] to estimate the Windkessel parameters can be described as follows:

This article has been accepted for publication in IEEE Transactions on Biomedical Engineering. This is the author's version which has not been fully edited and content may change prior to final publication. Citation information: DOI 10.1109/TBME.2025.3605189

4 IEEE TRANSACTIONS ON BIOMEDICAL ENGINEERING, VOL. XX, NO. XX, XXXX 2025

Step (1): Compute the total resistance R_{total} and the total capacitance C_{total} by the following electrical relationship,

$$R_{\text{total}} = \frac{P_m}{Q_{\text{total}}}, \tag{5}$$

$$C_{\text{total}} = d(V_b)/dP, \tag{6}$$

where $R_{\text{total}} = R_p + R_d$. P_m is the mean arterial pressure (MAP) calculated by the weighted systolic (SBP) and the diastolic (DBP) blood pressures as $(\text{SBP} + 2\text{DBP})/3$. Q_{total} is the total cerebral volumetric blood flow. $V_b(t)$ is the total blood volume of the systemic arteries.

Step (2): Distribute R_{total} and C_{total} to each outlet using the following formulas,

$$R^k = R_{\text{total}}\frac{\sum(d^k)^3}{(d^k)^3}, \tag{7}$$

$$C^k = C_{\text{total}}\frac{\sum A^k}{A^k}, \quad k = 1,...,N, \tag{8}$$

where d^k and A^k are the diameter and area of the k–th artery outlet, respectively. The exponent 3 in Eq. (7) is adopted following the formulation in Taylor et al. [33], where flow resistance is assumed to scale with the cube of vessel diameter. N is the total number of the outlets.

The method based on Eq. (7) and Eq. (8) works well for many applications, however, most of the reconstructed outlet have similar diameters and areas in diameter in practice subject to the image resolution, and the number of outlets as well as their distribution are easily affected by the image quality. To improve the assignment of the Windkessel parameters in Step(2), we introduce a new method based on the vessel's functional region instead of the geometric features of the outlet, such as the diameter and area.

Step (2′): We first classify the major branches of the cerebral vessels into 7 regions $D^i, i = 1,...,7$, including Left ACA, Right ACA, Left MCA, Right MCA, Left PCA, Right PCA and the other arteries. Then, according to the distribution of the total cerebral blood flow in the individual arteries based on population statistics of normal samples, and combined with the patient-specific cerebrovascular tree (the fetal-type of the Circle of Willis [34]), we can obtain the individual flow rate Q^i to each region D^i,

$$Q^i = \alpha_i Q_{\text{total}}, \quad i = 1,...,7. \tag{9}$$

where α_i is the percentage of the total CBF for D^i published in [35]. Fig. 2 presents the distribution of total CBF for each region in a case with a specific Circle of Willis. It is important to note that this population-based CBF distribution does not fully capture individual variability or pathology-specific flow changes. It serves as an approximate substitute when subject-specific data are unavailable, but future work may incorporate individualized imaging.

Additionally, CBF ultimately reaches brain tissue to support its various physiological activities, making the distribution of CBF among major cerebral arteries intrinsically linked to the individual brain tissues they supply. This distribution is further correlated with the physiological parameters of the corresponding brain functional areas, such as volume and activity. Neuroscience has now developed detailed vascular
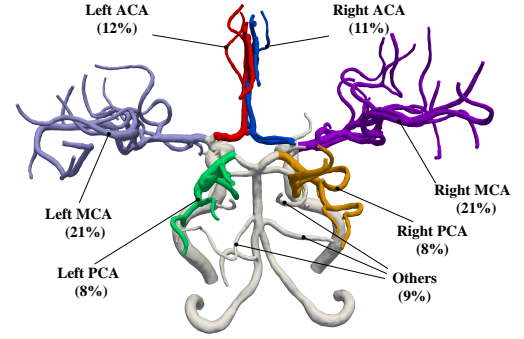

Fig. 2: Cerebral outlet classification. Vessels are color-coded according to their assigned functional regions. Blood flow allocation to each region is determined by coupling population-based total CBF distribution data with the patient-specific cerebrovascular anatomy. Values in brackets represent the mean regional CBF proportions reported for the general population with a complete Circle of Willis [35].

territory maps that correlate finely detailed brain tissue functional areas—including the cerebral cortex, gray matter, and white matter—with the corresponding vasculature [36], as shown in Fig. 3. These maps provide valuable tools for setting quantitative, individualized boundary conditions. However, current CBF simulation studies primarily use medical imaging, like MRI, for the 3D geometric reconstruction of cerebral arteries, overlooking other rich, subject-specific information highly relevant to hemodynamics, such as brain tissue and functional regions. To address this issue, future research will require substantial work to investigate the relationships among blood flow distribution, vasculature, and brain tissue functional areas, thereby providing accurate boundary conditions for CBF simulations and enhancing their precision.

Step (3): For each region D^i, we calculate the sub-resistance R^i and sub-capacitance C^i according to the parallel characteristics of the resistance,

$$R^i = \frac{R_{\text{total}}Q_{\text{total}}}{Q^i} = \frac{R_{\text{total}}}{\alpha_i}, \quad i = 1,...,7, \tag{10}$$

$$C^i = d(V_b)/dP. \tag{11}$$

Step (4): In each region D^i, the resistance and capacitance of the individual outlet j are as the function of the corresponding outlet's diameter d^j and area A^j,

$$R^j = R^i\frac{\sum(d^j)^3}{(d^j)^3}, \tag{12}$$

$$C^j = C^i\frac{\sum A^j}{A^j}, \quad j = 1,...,n, \tag{13}$$

where n is the number of outlets in region D^i.

D. Numerical solver and software

The incompressible Navier-Stokes equations Eq. (1) are discretized by a stabilized P_1–P_1 finite element method and a second-order backward differentiation for the spatial and temporal discretization, respectively. The computational domain is covered by an unstructured tetrahedral grid, and the resulting
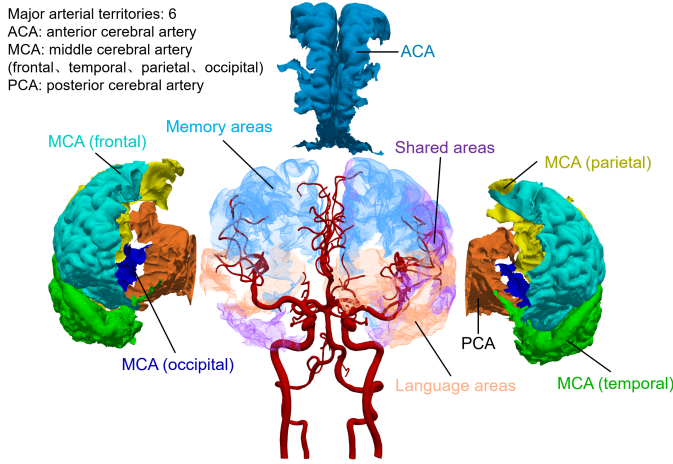
Fig. 3: Schematic diagram illustrating the major cerebral vessels and their distribution of blood flow to downstream primary brain tissue regions and secondary subdivided functional areas, based on the vascular territory map. Brain tissue can be initially divided into regions corresponding to major blood vessels based on their locations, such as the frontal, temporal, parietal, and occipital lobes. Subsequently, within each region, it can be further subdivided into different functional areas, such as language areas, visual processing areas, motor cortex, and sensory regions, based on their functionality. This information can be obtained synchronously with medical imaging used for artery reconstruction and can be utilized in subsequent studies to capture a more individualized CBF distribution.

large, sparse, nonlinear system is solved by a Newton-Krylov-Schwarz (NKS) solver [37].

In the NKS solver, the relative tolerances for the nonlinear and linear solvers are set to 1.0×10^{-6} and 1.0×10^{-4}, respectively. The domain decomposition uses an overlapping Schwarz method with an overlap size of $\delta = 2$. Incomplete LU factorization with fill level $\ell = 1$ is applied as a preconditioner. A restarted GMRES(k) algorithm with a maximum of $k = 400$ iterations is employed to efficiently solve the linear systems arising at each Newton step. More details on the discretization and solver are available in [38], [39].

The parallel software is developed on top of the open-source package PETSc (Argonne National Laboratory) and has recently been successfully applied in blood flow simulations [40]–[42]. ParaView (Kitware, Inc.) is employed for the visualization of the flow field. All simulations were performed on a cluster of computers and each computing node consists of two 12-core Intel Xeon E5-2692 v2 2.6GHz processors and 64 GB RAM.

III. RESULTS

In this section, we first list the parameters of the inflow and outlet boundary conditions. Then a grid independence study is performed to understand the dependence of computed flow field on the refinement of the mesh. Finally, we present a validation study to compare the results from the proposed functional region-based approach and the traditional outlet area-based approach, using the clinically measured velocity field with

TCD ultrasound. The total simulation time T corresponds to one cardiac cycle, determined by the subject's heart rate, and the time step is set to $\Delta t = 0.01$ s.

TABLE I: Some clinically measured data of the patient to be used in the numerical calculation and validation.

Inlet	Left ICA	Right ICA	Left VA	Right VA
Time-averaged TCD Measured Velocity (cm/s)	59.42	56.94	25.36	24.90
Inlet Area (cm^2)	0.25	0.22	0.15	0.13
Time-averaged Inflow Rate (cm^3/s)	15.08	12.62	3.79	3.19

Table I provides the patient data obtained from the TCD ultrasound and medical images for the numerical simulations including the inlet areas, time-averaged spectral velocities, and area-averaged flow rates on the corresponding inlets. We decompose the cerebral artery into a union of 7 connected, non-overlapping functional regions including the Left ACA, Right ACA, Left MCA, Right MCA, Left PCA, Right PCA and the other arteries, as shown in Fig. 2. For each of the 7 regions, we list the resistance, the number of outlets, and other information in Table II. The total number of outlets and their respective areas are derived from the reconstructed cerebral network. The distributions of cerebral blood flow, denoted as CBF^A (outlet area-based approach) and CBF^F (functional region-based approach), across the regions are determined using the area ratio and Eq. (9), respectively. The resistance of each region is determined using Eq. (10).

TABLE II: Characteristics of the seven functional regions.

D^i	#O	A_{total}	$\bar{A}$	CBF^A	R^A_{total}	$\overline{R}^A$	CBF^F	R^F_{total}	$\overline{R}^F$
Left ACA	6	7.069	1.178	13.0%	54370	326223	13.5%	52085	312510
Right ACA	6	7.408	1.235	13.6%	51762	310571	13.5%	52085	312510
Left MCA	16	11.312	0.707	20.8%	33706	539292	22.3%	31602	505632
Right MCA	15	10.235	0.682	18.9%	37449	561729	22.3%	31602	474030
Left PCA	4	3.405	0.851	6.3%	111832	447328	9.0%	78128	312512
Right PCA	8	4.380	0.548	8.1%	87666	701327	9.0%	78128	625024
Others	12	10.469	0.872	19.3%	36537	438449	10.4%	68047	816564
Total	67	54.278	0.810	100%	7043	-	100%	7043	-

Notes: D^i: the ith region; #O: the number of outlets in D^i; A_{total}: the total areas of outlets in D^i with unit mm^2; $\bar{A}$: the averaged area of outlet in D^i with unit mm^2; Superscripts A and F represent using the area-based and functional region-based assignment, respectively. CBF^A and CBF^F: the percentage of cerebral blood flow through region D^i; R^A_{total} and R^F_{total}: the total resistance of outlets in D^i with unit dyne $\cdot$ s/cm^5; $\overline{R}^A$ and $\overline{R}^F$: the averaged resistance of outlets in D^i with unit dyne $\cdot$ s/cm^5.

A. Mesh selection

The accuracy of the numerical simulation depends critically on the mesh on which the problem is discretized. In theory, the solution is more accurate if the mesh is refined, but the cost (or computational time) increases drastically. Therefore, it is important to select a mesh that is fine enough to offer an accurate solution but not too fine to waste computing resources. We consider three meshes with different maximum mesh sizes in the fluid domain and on the vascular wall, and the detailed mesh information are presented in Table III. To visualize the numerical solution, we select 7 monitoring points as marked in Fig. 4, and the velocity magnitude and pressure values for an entire cardiac cycle are plotted for each of the three meshes.

This analysis aims to understand how the computational results are influenced by the choice of mesh.

TABLE III: Information of three meshes used in the numerical simulations.

Mesh	Maximum Size in Fluid Domain (mm)	Maximum Size on Vascular Wall (mm)	Total Number of Elements	Degrees of Freedom
M1	1.20	0.35	2.3×10^6	1.7×10^6
M2	0.75	0.20	1.7×10^7	1.3×10^7
M3	0.60	0.12	2.8×10^7	2.0×10^7

Fig. 4 presents a comparison of velocity and pressure profiles based on both local assessments at seven monitoring points and global hemodynamic metrics across the computational domain. Local comparison at seven points showed negligible pressure differences between meshes M2 and M3 (max error $< 0.6\%$), while velocity errors were slightly higher in regions like the LMCA (mean error 7.78%). Globally, M2 closely matched M3, with relative errors under 0.4% for both pressure and velocity. In contrast, coarser mesh M1 showed up to 5.75% error in pressure and 3.31% in velocity. Given this balance of accuracy and cost, M2 was used for all simulations. For this mesh, the average walltime per timestep was 166.3 seconds, resulting in a total runtime of approximately 4.62 hours for one full cardiac cycle using 720 CPU cores.

B. Pressure and velocity

We conduct a comparative analysis between computed pressure and velocity values and data measured by TCD for a cardiac cycle. We examine seven specific locations for this comparison, including the BA, the left and right ACA, the left and right MCA, and the left and right PCA. The precise locations are indicated in Fig. 1.

We first present the pressure curves during a cardiac cycle at the cross sections of seven locations in Fig. 5. As TCD does not provide direct pressure measurements, we employ an approach known as "CFD with TCD distribution" to derive pressure values based on TCD measured data. This method involves converting TCD measured velocities into cerebral blood flow distribution, as specified by Eq. (9). Subsequently, we establish outlet boundary conditions using Eq. (10–13), and obtain the simulated pressure values. In Fig. 5, the red curves are from "CFD with TCD distribution" approach, the blue curves are from the proposed method whose resistance values are computed with proposed functional region-based approach, and the black curves are from the classical area-based approach. At each location, the computed pressure is spatially averaged over the cross section at the measurement location. We observe that the differences in the pressure waveforms obtained by the two computational methods are small, with the main disparities occurring in the end-systolic phase and no noticeable differences during the diastole phase. The relative differences in pressure on the seven locations are: 1.7%, 1.5%, 1.6%, 0.7%, 0.0%, 0.9%, and 1.1%, respectively.

Fig. 6 illustrates the comparison of transient spatially-averaged velocity profiles obtained using the proposed functional region-based approach, the area-based approach, and TCD measurements.

In terms of velocity waveforms, we can observe that the differences in velocities among the three methods are more pronounced compared to the pressure comparison. In left ACA, the velocity waveforms obtained by both functional region-based approach and area-based approach are significantly different from the waveform measured by TCD. This deviation is likely due to several factors. First, the left ACA has pronounced curvature and originates at a bifurcation, which may lead to skewed velocity profiles and recirculation zones [43], features poorly captured by TCD, which assumes axial flow. Second, geometric inaccuracies in segmentation (e.g., diameter or curvature) can significantly affect local hemodynamics. Third, our framework assigns resistance based on target flow distribution, without explicitly subtracting the proximal resistance due to the CFD domain. As a result, the total outlet resistance may slightly overestimate the intended downstream resistance, potentially leading to underestimation of local velocities. Although this approximation is commonly adopted in studies [20], [30], it may contribute to local mismatch, particularly in vessels like the ACA where geometric sensitivity is high. These factors may together explain the larger mismatch observed in this region, despite good global agreement. Local streamlines in Fig. 7 further illustrate the flow complexity. Additionally, the streamline visualizations reveal the presence of vortices, particularly at bifurcations such as the ACA and MCA junctions. These vortical structures are consistent with previously reported vortex dynamics in cerebral arteries [44], [45], suggesting that local flow instability may contribute to the variations we observed.

In terms of mean velocity magnitudes, the relative differences between the area-based approach and TCD measurements on the seven locations (BA, left and right ACA, left and right MCA, and the left and right PCA) are: -0.3%, 56.8%, 71.5%, -0.2%, -24.9%, -22.7%, and -30.2%, respectively. When using functional region-based approach, the differences become 18.0%, 41.7%, 32.2%, 16.8%, -3.6%, 16.9%, and 5.2%, respectively. Our proposed functional region-based approach produced results that were more consistent with TCD measurements at 5 of the 7 monitoring locations: left and right ACA, Right MCA, and left and right PCA. Especially, at right ACA, right MCA, and right PCA, the functional region-based approach shows a significant improvement in matching with TCD measurements. More detailed velocity and further results comparisons are listed in Table V.

To assess the reliability of the simulation results, we evaluated both the consistency across multiple cardiac cycles and the sensitivity to the spatial distribution of inlet velocity profiles, using the functional region-based approach on mesh M2. Pressure and velocity waveforms were compared at seven monitoring locations, and the error metrics are summarized in Table IV. Between the first and fifth cardiac cycles, the mean relative errors remained below 1.0% for pressure and 0.4% for velocity at all sites, indicating that first-cycle results already approximate the periodic regime with reasonable accuracy. To evaluate inlet sensitivity, simulations using a uniform profile were compared against those using a parabolic profile, where the peak velocity is twice the mean. The mean absolute differences in pressure and velocity remained
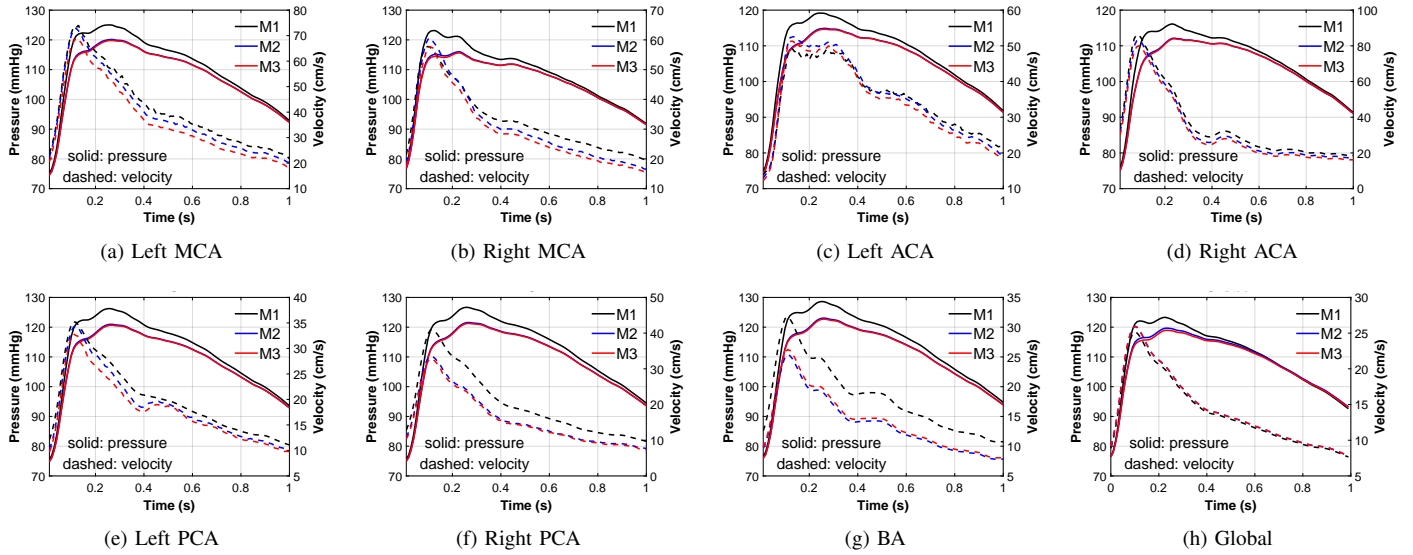
This article has been accepted for publication in IEEE Transactions on Biomedical Engineering. This is the author's version which has not been fully edited and content may change prior to final publication. Citation information: DOI 10.1109/TBME.2025.3605189

ZHENGZHENG YAN *et al.*: A FUNCTIONAL REGION-BASED APPROACH FOR THE NUMERICAL SIMULATION OF PATIENT-SPECIFIC CEREBRAL BLOOD FLOWS WITH CLINICAL VA

Fig. 4: Mesh independence test using unsteady velocity and pressure across three mesh sets, M1, M2 and M3. (a)–(g): seven measurement positions; (h): averaged across the entire flow domain.
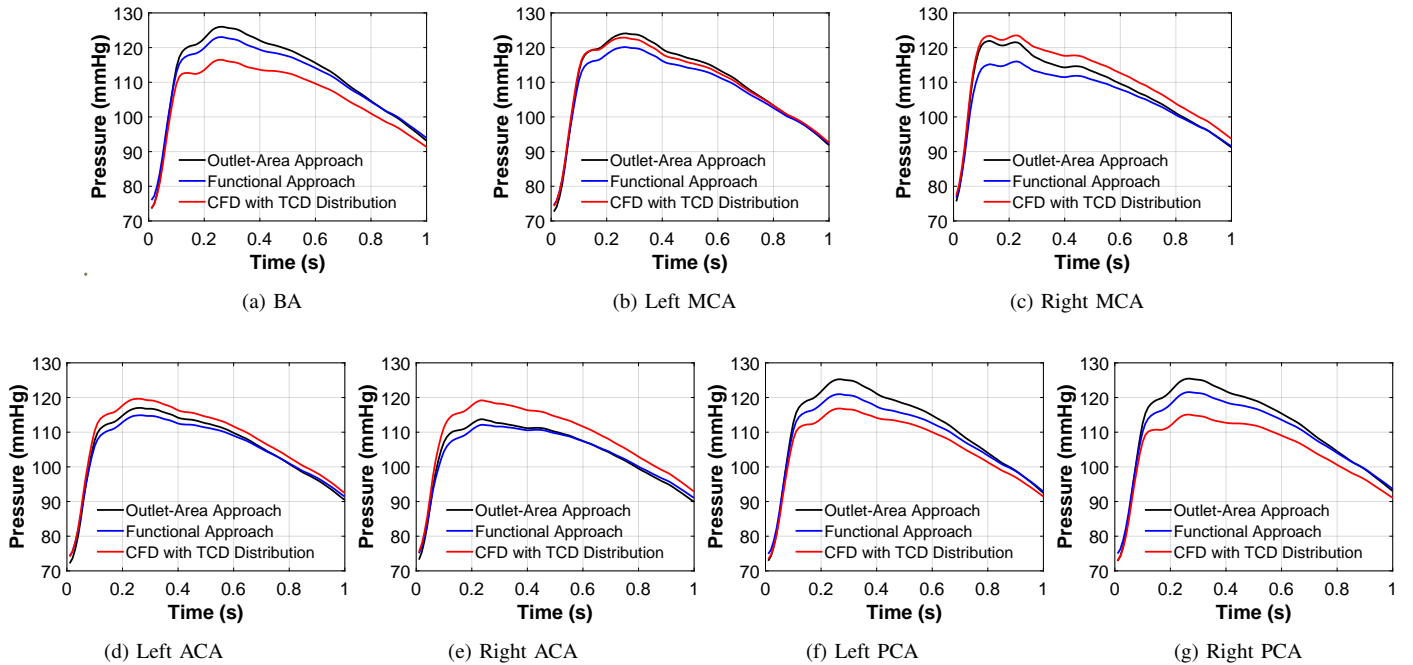

Fig. 5: Comparison of transient pressure profiles using area-based approach (black line), functional region-based approach (blue line), and CFD with TCD distribution approach (red line) in a cardiac cycle at seven measurement planes, as indicated in Fig. 1. The pressure values were area-averaged at the respective measurement planes.

below 0.91 mmHg (relative error $\leq 0.93\%$) and 0.81 cm/s (relative error $\leq 1.88\%$), respectively, confirming that adopting a uniform inlet profile introduces only minor discrepancies in intracranial pressure and velocity predictions.

C. Cerebral blood flow distribution

Patient-specific cerebral blood flow distribution is intimately related to brain function, for example, the flow asymmetries are interpreted as being related to functional lateralization of some aspects of attentional activation. The unique morphology of cerebral arteries is one reason why blood distribution varies among individuals. Therefore, we present a comparison of cerebral blood flow distribution calculated using velocities measured with TCD, simulated with the area-based and proposed functional-region based approach. The complementary data, including areas, velocities, and the total volume flow rate

(a) BA　　　(b) Left MCA　　　(c) Right MCA

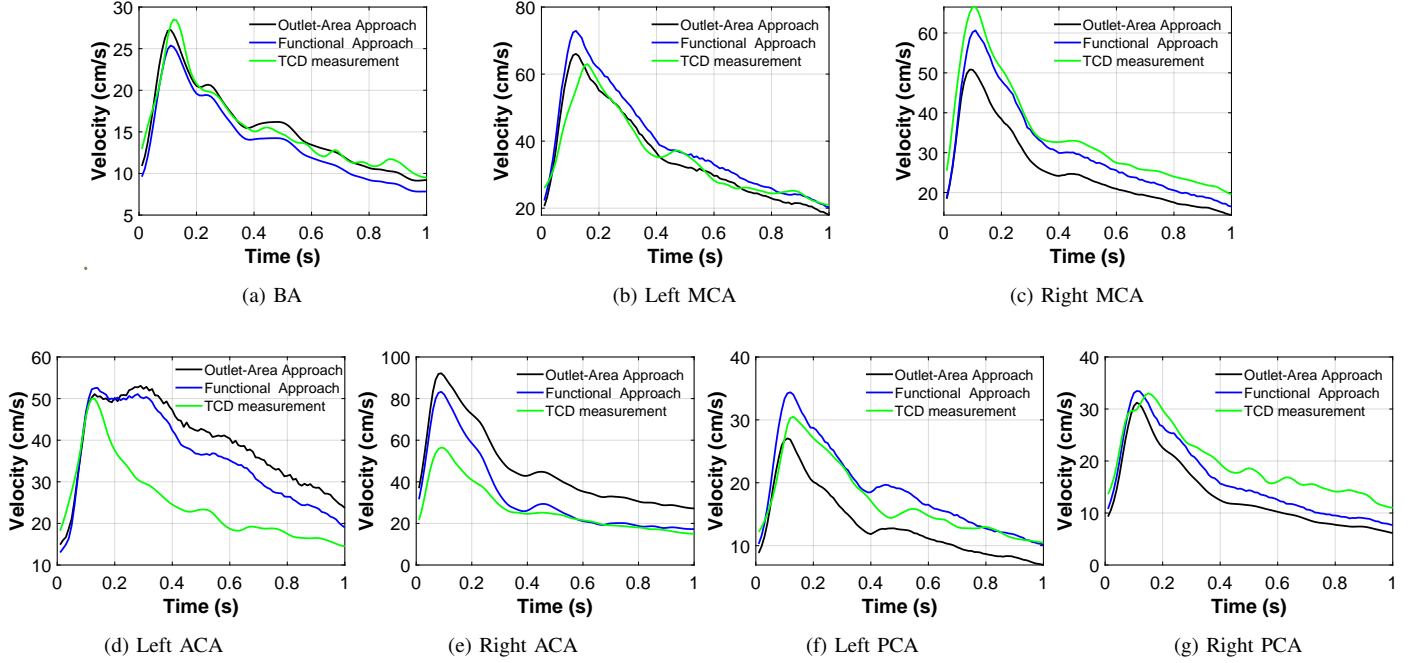(d) Left ACA　　　(e) Right ACA　　　(f) Left PCA　　　(g) Right PCA

Fig. 6: Comparison of the transient velocity profiles using area-based approach (black line), functional region-based approach (blue line), and TCD measurements (green line) in a cardiac cycle at seven measurement planes, as indicated in Fig. 1. The velocities were area-averaged at the respective measurement planes.
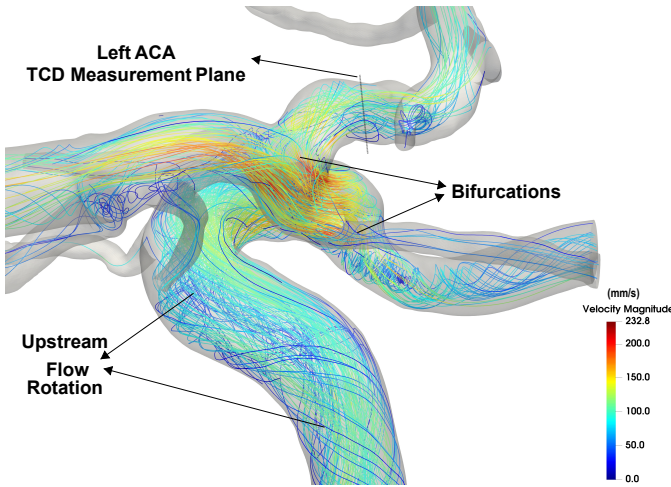

Fig. 7: Streamlines near the left ACA monitoring plane.

TABLE IV: Relative and absolute errors in blood pressure and flow velocity under two conditions: comparison between the first and fifth cardiac cycles, and comparison between uniform and parabolic flow profile boundary conditions.

Variable	Location	Cycle (First vs. Fifth)		Flow Profile (Uniform vs. Parabolic)	
		Mean Relative Error (%)	Mean Absolute Error	Mean Relative Error (%)	Mean Absolute Error
Pressure (mmHg)	BA	0.77	0.75	0.93	0.91
	Left ACA	0.83	0.78	0.88	0.83
	Left MCA	0.80	0.76	0.90	0.86
	Left PCA	0.79	0.76	0.91	0.88
	Right ACA	0.83	0.78	0.88	0.83
	Right MCA	0.81	0.78	0.87	0.84
	Right PCA	0.79	0.76	0.92	0.89
Velocity (cm/s)	BA	0.20	0.07	1.88	0.62
	Left ACA	0.20	0.12	1.34	0.81
	Left MCA	0.27	0.16	0.99	0.57
	Left PCA	0.37	0.11	1.24	0.36
	Right ACA	0.17	0.09	0.63	0.35
	Right MCA	0.26	0.13	0.89	0.46
	Right PCA	0.36	0.15	0.89	0.36

through the monitoring cross-sections, are listed in Table V. In this table, Q indicates the total volume flow rate through the monitoring cross-sections. Blood flow is also distributed to other vessels besides the 6 main cerebral arteries, which is why Q differs by approach even under the same inflow rate.

To clearly illustrate the advantages of our method, we compared the blood flow distribution among the six main blood vessels using the area-based approach, the functional region-based approach, and the TCD measurements in Fig. 8. The blood flow distribution is represented as the ratio of the flow through each cross-section to the total flow, denoted as

Q. As depicted in Fig. 8, the maximum percentage difference between the functional region-based calculations and the TCD measurements was -4.5% in Right MCA. Meanwhile, the differences were 3.5%, 1.7%, 0.2%, -4.5%, 0.1%, and -1.1% in left and right ACA, left and right MCA, and left and right PCA, respectively. Notably, there was remarkable agreement between our calculations and the TCD data for the left MCA and the left and right PCA. These results suggest that the functional region-based approach exhibits significantly closer agreement with the TCD measurements compared to the area-based approach.

TABLE V: Comparison of cerebral blood flow distribution among the area-based approach, our proposed functional region-based approach, and TCD measurements.

Position		Left ACA	Right ACA	Left MCA	Right MCA	Left PCA	Right PCA	Total Q
Monitoring Cross-section Area (mm^2)		7.285	5.142	8.248	9.371	7.083	7.13	-
Functional Region-based Approach	Velocity (mm/s)	352.8	358.0	413.0	329.6	200.5	203.6	13777.9
	Flow rate (mm^3/s)	2570.1	1840.8	3406.4	3088.7	1420.1	1451.7	
	%Q	18.70%	13.40%	24.70%	22.40%	10.30%	10.50%	
Area-based Approach	Velocity (mm/s)	390.4	464.6	352.3	256.8	132.7	135.1	12448.4
	Flow Rate (mm^3/s)	2844.1	2389.0	2905.8	2406.5	939.9	963.3	
	%Q	22.80%	19.20%	23.30%	19.30%	7.60%	7.70%	
TCD Measurements	Velocity (mm/s)	248.9	270.8	353.5	342.1	171.5	193.5	11921.5
	Flow Rate (mm^3/s)	1813.2	1392.5	2915.7	3205.8	1214.7	1379.7	
	%Q	15.20%	11.70%	24.50%	26.90%	10.20%	11.60%	

Notes: Area: the area of the corresponding monitoring cross-section; Velocity: the time and area-averaged blood velocity magnitude on the corresponding monitoring cross-section; Flow rate: the time-averaged volume flow rate through the corresponding monitoring cross-section. Q: the total volume flow rate through the six monitoring cross-sections. %Q: flow distribution.
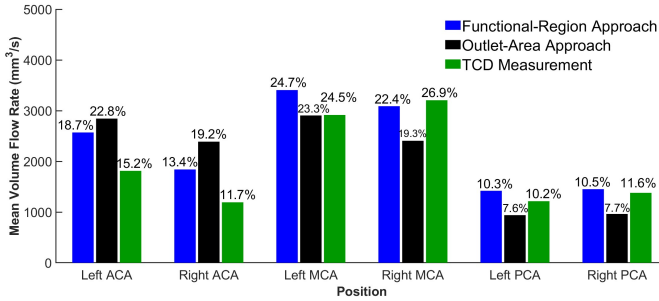

Fig. 8: Comparison of blood flow rate distribution. The height of the block represents the magnitude of the mean volume flow rate through the corresponding monitoring plane. The percentage indicates the distribution of flow rate in the six-outlet groups.

IV. DISCUSSION

The numerical experiments evaluate the functional region-based and area-based methods, comparing their performance in simulating pressure, velocity profiles, and blood flow distribution across a cardiac cycle at seven critical cerebral locations. These locations, including the BA, left and right ACA, MCA, and PCA, play key roles in cerebral hemodynamics, functioning as inflow channels, distribution points, or outlets that regulate and deliver blood to various brain regions.

The comparison of pressure profiles, illustrated in Fig.,5, shows minimal differences between the functional region-based and classical area-based methods. Notably, these differences are negligible during the diastolic phase, with minor discrepancies occurring primarily during the end-systolic phase. The maximum relative difference in computed pressure across the seven locations is 1.7%, indicating that both methods provide comparable accuracy in transient cerebral blood pressure simulations. This observation aligns with previous studies indicating that pressure profiles are generally less sensitive to variations in outlet boundary conditions than velocity [43], [46].

In contrast to the pressure results, velocity profiles exhibited more pronounced discrepancies and greater sensitivity to the choice of outlet boundary conditions. As emphasized by Vikström et al. [47], inaccurate outflow assumptions can significantly distort local velocity fields, particularly within the Circle of Willis. In our study, the relative differences in mean velocity magnitudes between the area-based approach and TCD measurements ranged from -30.2% to 71.5%. When using the functional region-based method, these differences were significantly reduced to a range of -3.6% to 41.7%. Furthermore, improved agreement with TCD measurements was observed at five out of the seven monitored locations, especially in the right ACA, right MCA, and right PCA. These results highlight the advantage of incorporating functional regional information for capturing localized hemodynamic behavior more accurately than traditional area-based approaches. The observed vortex patterns at bifurcations, particularly in the ACA, emphasize the role of local hemodynamics in shaping flow distribution and vessel wall stresses. Future studies could combine advanced imaging modalities, such as 4D Flow-MRI imaging, with computational models to improve both pressure estimation [48] and the quantification of vortex dynamics [49] in cerebral circulation.

In terms of periodicity, the pressure and velocity differences between the first and fifth cardiac cycles were negligible, with maximum mean relative errors of 0.83% and 0.37%, respectively. These results suggest that single-cycle simulations can yield representative results when computational resources are limited. Regarding the spatial distribution of inflow, while several studies [50]–[52] have emphasized the importance of using measured or Womersley-type inlet profiles in large-vessel simulations, our findings indicate that this factor is less critical in cerebral blood flow simulations. The anatomical distance

between the internal carotid artery and the intracranial vessels of interest likely allows sufficient flow development, reducing the influence of the initial velocity profile. This supports the practicality of using a uniform inlet assumption in patient-specific cerebral blood flow simulations, particularly when detailed velocity measurements are unavailable.

Cerebral blood flow distribution, a critical factor linked to brain function, varies significantly among individuals due to the unique morphology of cerebral arteries. The functional region-based method demonstrated superior performance compared to the area-based approach in predicting blood flow distribution. The maximum percentage difference between the functional region-based calculations and TCD measurements was -4.5% in the right MCA. This residual deviation may be due to a combination of factors. Minor geometric inaccuracies can disproportionately influence flow split, particularly in large vessels like the MCA where resistance depends strongly on diameter. In addition, population-based flow distributions may not reflect subject-specific variability. Anatomical asymmetries in the Circle of Willis or downstream branches may also shift flow in ways the model does not fully capture. Despite these limitations, differences for the other vessels ranged from -4.5% to 3.5%, with excellent agreement observed in the left MCA and both PCA branches.

Our results are consistent with prior studies emphasizing the importance of personalization in cerebrovascular CFD. Cebral et al. [53] demonstrated that the predictive accuracy of CFD models relies heavily on patient-specific anatomical and physiological inputs. More recently, McGuire et al. [54] used multi-modal imaging to derive individualized flow data for simulating arteriovenous malformations.

Beyond the area-based method, several other outlet modeling strategies exist, such as structured-tree impedance models [55] and autoregulatory Windkessel models [30]. Structured-tree impedance models approximate the downstream microcirculation using idealized branching trees under linear flow assumptions but are limited in capturing patient-specific anatomical variability. Autoregulatory Windkessel models adjust outlet resistance dynamically based on deviations from target pressures or flow rates. While physiologically sophisticated, these models typically rely on high-fidelity pressure measurements and require multiple iterations to reach convergence. In contrast, the proposed functional region-based approach assigns outlet parameters in a pre-computed manner using image-derived vascular topology and population-based cerebral perfusion data. This avoids the need for iterative tuning while maintaining reasonable physiological fidelity. Its simplicity make it well suited for individualized analysis and potential clinical application, especially in settings where full pressure data are not available.

V. LIMITATIONS

The primary limitation of this study is the reliance on data from a single subject. Given the absence of a comprehensive mathematical model describing cerebral blood flow regulation, the proposed method requires validation in larger cohorts to ensure generalizability. While the proposed method showed improved agreement with measured flow data in this case, the influence of physiological variability in inputs such as perfusion fractions and outlet diameters was not systematically analyzed. A sensitivity analysis evaluating how perturbations in these parameters affect key outputs, such as regional flow distribution or peak wall shear stress, will be important for quantifying model robustness. Such analysis will also inform how many additional cases may be required for broader validation in future studies.

Several sources of modeling and measurement uncertainty are also acknowledged. First, the spatial resolution constraints of clinical MRA may introduce diameter estimation errors greater than 10% for small vessels (diameter less than 2 mm), with the exact error depending on image settings and vascular geometry [56], [57]. Second, the use of rigid-wall and Newtonian assumptions may neglect arterial compliance and non-Newtonian blood behavior, which have been shown to affect intracranial hemodynamic metrics by more than 10% in intracranial CFD studies [58]. Third, TCD-based validation introduces further uncertainty due to insonation angle variation and operator dependence, with reported velocity errors of 10–20% [29]. Additionally, full multi-cycle verification should be considered to confirm periodic stability, as suggested by Mariotti et al. [59]. Future studies will explore the use of synthetic 4D Flow-MRI datasets to provide full-field velocity reference data and assess the sensitivity of model predictions to these sources of uncertainty.

Finally, although the simulations benefit from parallelization on high-performance computing systems, full 3D cerebral blood flow simulations remain computationally intensive: requiring approximately 4.6 hours per cardiac cycle on 720 CPU cores. This limits applicability in real-time clinical settings. However, the method is feasible for use in batch-mode analysis for research or pre-surgical planning, and could be accelerated in the future through the design of more efficient solvers.

VI. CONCLUSIONS

This study introduces a functional region-based approach to enhance parameter assignment in the widely used Windkessel model for simulating patient-specific cerebral blood flow. In contrast to the current area-based method, which only considers the geometric characteristics of outlets, the improved functional region-based method incorporates both functional characteristics and the cerebral vasculature. By pre-allocating blood flow to the main vessels based on population-averaged distributions and subsequently distributing parameters to downstream outlets according to their corresponding areas, this approach provides a more comprehensive and physiologically relevant simulation of cerebral hemodynamics. Compared to the traditional area-based approach, the functional region-based method yields results that align more closely with clinical Transcranial Doppler measurements, particularly in terms of blood flow distribution in the primary cerebral arteries. A key advantage of this method is its ability to reduce simulation errors resulting from incomplete and imprecise vessel geometry representations, which are common limitations due to reliance on medical image resolution and operator expertise. Nonetheless, validation remains limited

to a single case and should be regarded as preliminary. Broader clinical studies across diverse patient populations are needed to assess the generalizability and clinical relevance of the proposed approach. Future work will investigate using detailed vascular territory maps and advanced flow imaging techniques to obtain blood flow distribution information for major vessels and even more downstream branches, thereby enhancing the accuracy of cerebral blood flow simulations.

REFERENCES

[1] L. Pantoni, "Cerebral small vessel disease: From pathogenesis and clinical characteristics to therapeutic challenges," *The Lancet Neurology*, vol. 9, no. 7, pp. 689–701, 2010.

[2] Y. Chen et al., "Non-invasive assessment of intracranial wall shear stress using high-resolution magnetic resonance imaging in combination with computational fluid dynamics technique," *Fundamental Research*, vol. 2, no. 2, pp. 329–334, 2022.

[3] A. R. Bateman et al., "Computational fluid dynamic simulation of the cerebral venous system in multiple sclerosis and control patients: are hemodynamic variances evident in multiple sclerosis?," *IEEE Transactions on Biomedical Engineering*, vol. 72, no. 3, pp. 1021–1030, 2025

[4] M. Mirramezani et al., "A distributed lumped parameter model of blood flow," *Annals of Biomedical Engineering*, vol. 48, no. 12, pp. 2870–2886, 2020.

[5] J. A. Claassen et al., "Regulation of cerebral blood flow in humans: physiology and clinical implications of autoregulation," *Physiological Reviews*, vol. 101, no. 4, pp. 1487–1559, 2021.

[6] K. Malhotra and D. S. Liebeskind, "Collaterals in ischemic stroke," *Brain Hemorrhages*, vol. 1, no. 1, pp. 6–12, 2020.

[7] T. Thirugnanachandran et al., "Anterior cerebral artery stroke: role of collateral systems on infarct topography," *Stroke*, vol. 52, no. 9, pp. 2930–2938, 2021.

[8] N. Westerhof et al., "The arterial windkessel," *Medical & Biological Engineering & Computing*, vol. 47, no. 2, pp. 131–141, 2009.

[9] H. Huang et al., "In vitro identification of four-element Windkessel models based on iterated unscented Kalman filter," *IEEE Transactions on Biomedical Engineering*, vol. 58, no. 9, pp. 2672–2680, 2011.

[10] J. Liu et al., "Functional assessment of cerebral artery stenosis: A pilot study based on computational fluid dynamics," *Journal of Cerebral Blood Flow & Metabolism*, vol. 37, no. 7, pp. 2567–2576, 2017.

[11] T. Kang et al., "Effects of progressive carotid stenosis on cerebral haemodynamics: aortic-cerebral 3D patient-specific simulation," *Engineering Applications of Computational Fluid Mechanics*, vol. 15, no. 1, pp. 830–847, 2021.

[12] R. M. Padmos et al., "Coupling one-dimensional arterial blood flow to three-dimensional tissue perfusion models for *in silico* trials of acute ischaemic stroke," *Interface Focus*, vol. 11, no. 1, p. 20190125, 2021.

[13] S. Acosta et al., "An effective model of cerebrovascular pressure reactivity and blood flow autoregulation," *Microvascular Research*, vol. 115, pp. 34–43, 2018.

[14] T. W. Secomb and A. R. Pries, "The microcirculation: physiology at the mesoscale," *The Journal of Physiology*, vol. 589, no. 5, pp. 1047–1052, 2011.

[15] Z. Tong et al., "A multiscale model of cerebral autoregulation," *Medical Engineering & Physics*, vol. 95, pp. 51–63, 2021.

[16] R. Gul, "Mathematical modeling and sensitivity analysis of lumped-parameter model of the human cardiovascular system," Ph.D. thesis, Freie Universität Berlin, Berlin, 2016.

[17] S. Zhou et al., "Ultrasound-based method for individualized estimation of central aortic blood pressure from flow velocity and diameter," *Computers in Biology and Medicine*, vol. 143, p. 105254, 2022.

[18] L. Grinberg et al., "Large-scale simulation of the human arterial tree," *Clinical and Experimental Pharmacology and Physiology*, vol. 36, no. 2, pp. 194–205, 2009.

[19] R. Lal et al., "Non-invasive blood flow features estimation in cerebral arteries from uncertain medical data," *Annals of Biomedical Engineering*, vol. 45, no. 11, pp. 2574–2591, 2017.

[20] R. Chen et al., "A parallel non-nested two-level domain decomposition method for simulating blood flows in cerebral artery of stroke patient," *International Journal for Numerical Methods in Biomedical Engineering*, vol. 36, no. 11, 2020.

[21] J. Zhou et al., "High-resolution cerebral blood flow simulation with a domain decomposition method and verified by the TCD measurement," *Computer Methods and Programs in Biomedicine*, vol. 224, p. 107004, 2022.

[22] D. Attwell et al., "Glial and neuronal control of brain blood flow," *Nature*, vol. 468, no. 7321, pp. 232–243, 2010.

[23] D. A. Hartmann et al., "Pericyte control of blood flow across microvascular zones in the central nervous system," *Annual Review of Physiology*, vol. 84, no. 1, pp. 331–354, 2022.

[24] S. M. Black et al., "Reconstruction and validation of arterial geometries for computational fluid dynamics using multiple temporal frames of 4D Flow-MRI magnitude images," *Cardiovascular Engineering and Technology*, vol. 14, pp. 655–676, 2023.

[25] S. M. Black et al., "Calibration of patient-specific boundary conditions for coupled CFD models of the aorta derived from 4D Flow-MRI," *Frontiers in Bioengineering and Biotechnology*, vol. 11, p. 1178483, 2023.

[26] A. G. Morgan et al., "4D flow MRI for non-invasive measurement of blood flow in the brain: A systematic review," *Journal of Cerebral Blood Flow & Metabolism*, vol. 41, no. 2, pp. 206–218, 2021.

[27] X. Wu et al., "Expanding the coronary tree reconstruction to smaller arteries improves the accuracy of FFR$_{CT}$," *European Radiology*, vol. 31, no. 12, pp. 8967–8974, 2021.

[28] L. Lan et al., "Sustaining cerebral perfusion in intracranial atherosclerotic stenosis: the roles of antegrade residual flow and leptomeningeal collateral flow," *Journal of Cerebral Blood Flow & Metabolism*, vol. 40, no. 10, pp. 2052–2062, 2020.

[29] J. Naqvi et al., "Transcranial Doppler ultrasound: A review of the physical principles and major applications in critical care," *International Journal of Vascular Medicine*, vol. 2013, p. 629378, 2013.

[30] M. S. Olufsen et al., "Dynamics of cerebral blood flow regulation explained using a lumped parameter model," *American Journal of Physiology-Regulatory, Integrative and Comparative Physiology*, vol. 282, no. 2, pp. R611–R622, 2002.

[31] I. Vignon-Clementel et al., "Outflow boundary conditions for 3D simulations of non-periodic blood flow and pressure fields in deformable arteries," *Computer Methods in Biomechanics and Biomedical Engineering*, vol. 13, no. 5, pp. 625–640, 2010.

[32] N. Xiao et al., "A systematic comparison between 1-D and 3-D hemodynamics in compliant arterial models," *International Journal for Numerical Methods in Biomedical Engineering*, vol. 30, no. 2, pp. 204–231, 2014.

[33] C. A. Taylor et al., "Computational fluid dynamics applied to cardiac computed tomography for noninvasive quantification of fractional flow reserve: scientific basis," *Journal of the American College of Cardiology*, vol. 61, no. 22, pp. 2233–2241, 2013.

[34] V. Kızılgöz et al., "Evaluation of Circle of Willis variants using magnetic resonance angiography," *Scientific Reports*, vol. 12, no. 1, p. 17611, 2022.

[35] L. Zarrinkoob et al., "Blood flow distribution in cerebral arteries," *Journal of Cerebral Blood Flow & Metabolism*, vol. 35, no. 4, pp. 648–654, 2015.

[36] D.-E. Kim et al., "Mapping the supratentorial cerebral arterial territories using 1160 large artery infarcts," *JAMA Neurology*, vol. 76, no. 1, pp. 72–80, 2019.

[37] X.-C. Cai et al., "Restricted additive Schwarz preconditioners with harmonic overlap for symmetric positive definite linear systems," *SIAM Journal on Numerical Analysis*, vol. 41, no. 4, pp. 1209–1231, 2003.

[38] R. Chen et al., "A parallel domain decomposition method for 3D unsteady incompressible flows at high Reynolds number," *Journal of Scientific Computing*, vol. 58, no. 2, pp. 275–289, 2014.

[39] Z. Yan et al., "Large eddy simulation of the wind flow in a realistic full-scale urban community with a scalable parallel algorithm," *Computer Physics Communications*, vol. 270, p. 108170, 2022.

[40] Z. Yan et al., "Impact of pressure wire on fractional flow reserve and hemodynamics of the coronary arteries: A computational and clinical study," *IEEE Transactions on Biomedical Engineering*, vol. 70, no. 5, pp. 1683–1691, 2022.

[41] Y. Liu et al., "Is invasive fractional flow measurement accurate in intracranial stenosis? A computational simulation study," *Journal of NeuroInterventional Surgery*, published online first: May 20, 2025, doi: 10.1136/jnis-2025-023342.

[42] Z. Yan et al., "A computational study of the connection between coronary revascularization and cardio-cerebral hemodynamics," *Computer Methods and Programs in Biomedicine*, vol. 263, p. 108667, 2025.

[43] K. Valen-Sendstad and D. A. Steinman, "Mind the gap: Impact of CFD solution strategy on prediction of intracranial aneurysm hemodynamics," *American Journal of Neuroradiology*, vol. 35, no. 3, pp. 536–543, 2014.

[44] X. Zhang, et al., "Middle cerebral arterial bifurcation aneurysms are associated with bifurcation angle and high tortuosity," *Journal of Neuroradiology*, vol. 49, no. 5, pp. 392–397, 2022.

[45] F. Mehregan, et al., "Doppler vortography: a color Doppler approach to quantification of intraventricular blood flow vortices," *Ultrasound in Medicine & Biology*, vol. 40, no. 1, pp. 210–221, 2014.

[46] H. Yi et al., "Using DFT on ultrasound measurements to determine patient-specific blood flow boundary conditions for computational hemodynamics of intracranial circulation," *Computers in Biology and Medicine*, vol. 175, p. 107897, 2024.

[47] A. Vikström et al., "Non-invasive assessment of cerebral perfusion pressure: Applied towards preoperative planning of aortic arch surgery with selective antegrade cerebral perfusion," *Journal of Biomechanics*, vol. 157, p. 111456, 2025.

[48] A. Kazemi, et al., "Relative pressure estimation from 4D flow MRI using generalized Bernoulli equation in a phantom model of arterial stenosis," *Magnetic Resonance Materials in Physics, Biology and Medicine*, vol. 35, pp. 733–748, 2022.

[49] K. Futami, et al., "Identification of vortex cores in cerebral aneurysms on 4D flow MRI," *American Journal of Neuroradiology*, vol. 40, no. 12, pp. 2111–2116, 2019.

[50] I. C. Campbell et al., "Effect of inlet velocity profiles on patient-specific computational fluid dynamics simulations of the carotid bifurcation," *Journal of Biomechanical Engineering*, vol. 134, no. 5, p. 051001, 2012.

[51] S. Bozzi et al., "Uncertainty propagation of phase contrast-MRI derived inlet boundary conditions in computational hemodynamics models of the thoracic aorta," *Computer Methods in Biomechanics and Biomedical Engineering*, vol. 20, no. 10, pp. 1104–1112, 2017.

[52] A. Mariotti et al., "Impact of the spatial velocity inlet distribution on the hemodynamics of the thoracic aorta," *Cardiovascular Engineering and Technology*, vol. 14, no. 5, pp. 713–725, 2023.

[53] J. R. Cebral et al., "Aneurysm rupture following treatment with flow-diverting stents: Computational hemodynamics analysis of treatment," *American Journal of Neuroradiology*, vol. 32, no. 1, pp. 27–33, 2011.

[54] L. S. McGuire et al., "Feasibility study for multimodal image-based assessment of patient-specific intracranial AVM hemodynamics," *Journal of Clinical Medicine*, vol. 14, no. 8, p. 2638, 2025.

[55] P. Reymond et al., "Validation of a one-dimensional model of the systemic arterial tree," *American Journal of Physiology-Heart and Circulatory Physiology*, vol. 297, no. 1, pp. H208–H222, 2009.

[56] L. C. Jordan et al., "Using novel magnetic resonance imaging methods to predict stroke risk in individuals with sickle cell anemia," *Hematology/Oncology and Stem Cell Therapy*, vol. 13, no. 2, pp. 76–84, 2020.

[57] J. J. Westenberg et al., "Vessel diameter measurements in gadolinium contrast-enhanced three-dimensional MRA of peripheral arteries," *Magnetic Resonance Imaging*, vol. 18, no. 1, pp. 13–22, 2000.

[58] K. M. Saqr et al., "What does computational fluid dynamics tell us about intracranial aneurysms? A meta-analysis and critical review," *Journal of Cerebral Blood Flow & Metabolism*, vol. 40, no. 10, pp. 2036–2051, 2020.

[59] A. Mariotti et al., "Hemodynamics and stresses in numerical simulations of the thoracic aorta: Stochastic sensitivity analysis to inlet flow-rate waveform," *Computers & Fluids*, vol. 230, p. 105123, 2021.